

# Compensating Image Distortions in a Commercial Relectron-Type Atom Probe

Martina Heller, Benedict Ott, Peter Felfer



# Compensating Image Distortions in a Commercial Reflectron-Type Atom Probe

Martina Heller<sup>1,2,\*</sup>, Benedict Ott<sup>1</sup>, and Peter Felfer<sup>1</sup>

<sup>1</sup>Department of Materials Science, Institute for General Materials Properties, Friedrich-Alexander Universität Erlangen-Nürnberg (FAU), Martensstr.5, Erlangen 91058, Germany

<sup>2</sup>Interdisciplinary Center for Nanostructured Films (IZNF), Cauerstr.3, Erlangen 91058, Germany

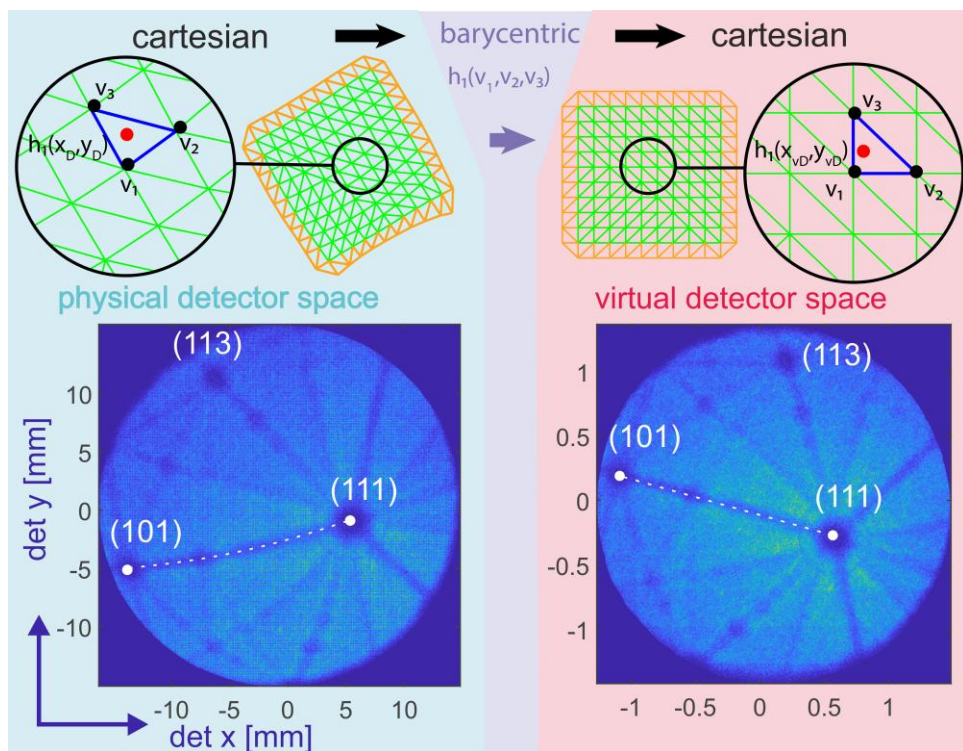
\*Corresponding author: Martina Heller, Email: martina.heller@fau.de

## Abstract

In atom probe tomography, the spatial resolution and accuracy of the data critically depend on the 3D reconstruction of the 2D detector data. Atom probes with a reflectron have an improved mass resolving power and must include a model of the imaging properties of the reflectron. However, for modern wide-angle reflectron instruments, these imaging properties are not trivial and need to be determined for the reflectron used. This is typically done by the instrument manufacturer, and due to the proprietary nature of the instrument design, the imaging properties are opaque to the user. In this paper, we provide a method to determine the imaging properties of a reflectron that can easily be carried out on commercial instrumentation. This method is used to provide the user with a transformation function from the provided detector data, which can already contain some corrections applied, to a virtual detector placed before the reflectron. From there on, 3D reconstructions can be carried out analogous to straight flight path instruments. Correction algorithms and reference data for Imago/CAMECA LEAP 3000, 4000, 5000, and 6000 series instruments are also provided.

**Key words:** APT data correction, atom probe, reflectron

## Graphical Abstract



Received: May 26, 2023. Revised: September 30, 2023. Accepted: May 25, 2024

© The Author(s) 2024. Published by Oxford University Press on behalf of the Microscopy Society of America. All rights reserved. For commercial re-use, please contact [reprints@oup.com](mailto:reprints@oup.com) for reprints and translation rights for reprints. All other permissions can be obtained through our RightsLink service via the Permissions link on the article page on our site—for further information please contact [journals.permissions@oup.com](mailto:journals.permissions@oup.com).

## Introduction

Atom probe tomography (APT) is a 3D spatially resolved mass spectrometry method based on time-of-flight measurements of ions emitted from a solid sample by means of an electrostatic field (Müller et al., 1968; Blavette et al., 1993; Gault et al., 2012a). Very often this measurement is done using voltage pulses to trigger the field evaporation. Historically this was the dominant way to trigger field evaporation in APT, even though in recent years lasers have been used frequently after the introduction of short pulsed lasers (Kellogg & Tsong, 1980; Gault et al., 2006). When voltage pulses are used to trigger field evaporation, variations in ion energy are observed due to the finite duration of the pulse. These energy variations are causing a variation in flight time and thus degradation in mass resolving power, lowering the ability to differentiate between ions of similar mass-to-charge ratios. (Meisenkothen et al., 2016) The ion energy is not picked up by the currently used detection schemes. This problem was known early on in the development of atom probe instrumentation. It was, e.g., compensated by using longer flight distances in Poschenrieder L lenses or other lensing systems (Poschenrieder, 1972).

With the advent of spatially resolved detectors, the need for energy compensation schemes that preserve the spatial distribution of the ions arose. To this end, electrostatic reflectron mirrors were employed by Waugh et al. (1992) and Cerezo et al. (1998). These mirrors consist of a series of electrodes, creating a reflecting field through a series of high-transparency metal mesh grids, in which ions with greater energy penetrate deeper. Using such devices, the reachable mass resolution ( $\Delta m/m$ ) of atom probe instruments grew to  $> 1,000$  full width at half maximum. In early implementations, the solid angle that the detector covered was low, so flat reflectron mirrors, sitting close to the optical axis of the instrument, could be employed. These reflectrons did not require a significant amount of position correction. With the introduction of wide-angle atom probes (Panayi, 2006), covering large solid angles, wide-angle reflectrons with curved meshes were developed by the atom probe group at Oxford University and commercialized by Oxford Nanoscience. After the merger of Oxford Nanoscience with the original company marketing microelectrode atom probes, Imago (now part of CAMECA), they are currently also widely used in the LEAP series of atom probe instruments.

**Figure 1** schematically shows the difference between a conventional straight flight path atom probe and a reflectron-type atom probe. In a straight flight path atom probe, the ions are field-evaporated by an electric field between the specimen and a counter electrode, called the local electrode in the Imago/CAMECA LEAP instrument series, due to its close proximity to the specimen (typ. ca.  $50 \mu\text{m}$ ; Nishikawa & Kimoto, 1994; Kelly et al., 1996). The ions then pass through a near field-free drift region of several centimeters to several tens of centimeters in length until they impact on a 2D time-resolved detector. In the case of reflectron-fitted instruments, the ions are also field-evaporated by the field between the specimen and counter electrode, but once they are past the counter electrode, they enter the reflectron, where a carefully shaped electric field is present that reflects them back out, while also focusing them.

According to the manufacturer, approximately two-thirds of the 100 or so Imago/CAMECA instruments currently in service use a reflectron as it increases the mass resolving power

not just when using voltage pulsing but also when using pulsed-laser APT, as it significantly prolongs the flight time of the ions over instruments without electrostatic optical elements. This also increases the mass resolving power, proportional to the increase in flight time. On the other side, reflectron-equipped instruments have a decreased detection efficiency due to the finite transparency of the meshes. The reflectron covers a large solid angle and projects strong off-axis, which introduces significant imaging distortions. These imaging distortions are corrected by the proprietary data processing software from the manufacturer; however, this process is opaque to the user. With the \*.epos file format and its successors, provided in the data processing software suites by CAMECA, the user has access to the reconstructed  $x$ ,  $y$ , and  $z$  coordinates of the ions/atoms, including any reflectron correction. In addition, the file grants access to the detector  $x$  and  $y$  coordinates. These seem largely uncorrected and show the image distortions caused by the reflectron, even though the authors cannot rule out that some corrections are present in the data. Importantly, due to the distortions, these “raw” coordinates are not suitable as the basis of 3D reconstruction or other analyses.

In this paper, we therefore present a method for atom probe users to create their own reflectron calibration, to “un-distort” the projection of the provided detector data from reflectron instruments. It works by using a custom-made grid as a shadow mask, to create a controlled reference image at a known location, which is then recorded including the imaging distortions introduced by the reflectron. From this distorted image of the grid, an affine transformation is created using a triangulated reference mesh and a barycentric coordinate transformation based on a piecewise linear approximation. Using this method, virtual detector coordinate locations at the location of the grid can be calculated which in turn can be used for APT reconstruction. This will allow the users to work with data from their reflectron-equipped instruments as if they were in straight flight path configuration and carry out any analysis and data treatment that requires undistorted ion hit positions. This includes the use of advanced APT reconstruction and reconstruction calibration schemes (Gault et al., 2009; Beinke et al., 2016; Felfer & Cairney, 2016; Fletcher et al., 2022; Ling et al., 2022) and APT crystallography (Gault et al., 2012b).

## Materials and Methods

### Experimental Setup

To determine the imaging properties of the reflectron, the experimental setup was created with a known shadow image in the path of the ions at a position before the reflectron. This shadow image is created by a grid which was designed to fit into the local electrode pucks underneath the local electrode cone. This means it sits at a measured distance of  $3.5 \text{ mm}$  from the entrance aperture of the local electrode shown in **Figure 2a**. The grid is made from a  $25 \mu\text{m}$  thick stainless steel foil which was cut with a 3D-MICROMAC® microPREP™ PRO (3D-Micromac AG) laser ablation system.

The pitch of the grid is  $278 \mu\text{m}$ , with a total diameter of  $8 \text{ mm}$  (**Fig. 2b**). This is fine enough to justify linear distortion approximations between the grid bars. The grid also had alignment markers marking the grid center. The grid is mounted in a local electrode puck, by loosening the screw that holds the electrode cone and placing the grid beneath.

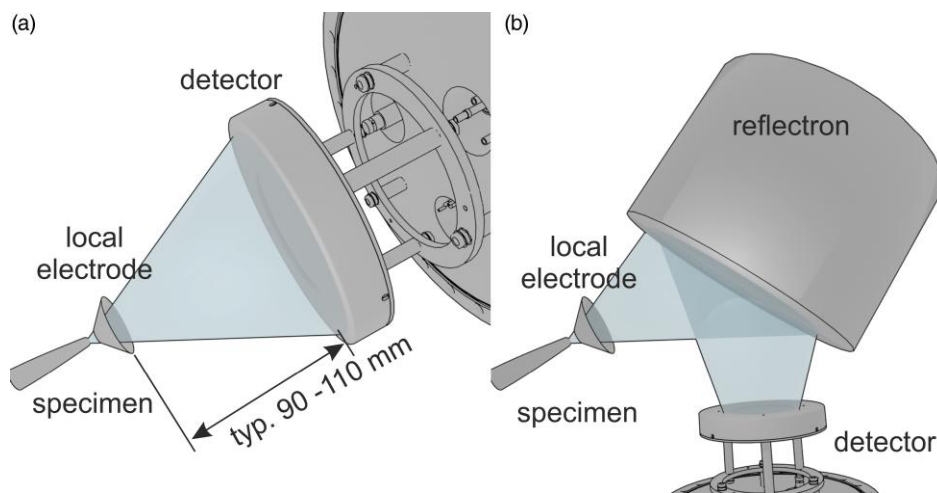


**Fig. 1.** (b) Experimental setup of a reflectron-based tomographic atom probe compared to a conventional, straight flight path atom probe in (a).

Tightening the screws holds the grid in place. Since there are no means to precisely align the grid during installation, the grid's rotation with respect to the edge of the puck and position with respect to the local electrode cone were determined from photographic images after installation (Fig. 2c). All data presented here that contain a shadow image of the grid were acquired with the same counter electrode and grid that was sent to different labs. The grid was never moved or removed, creating a consistent setup.

Using this setup, data sets from aluminum (Al), silicon (Si), and tungsten (W) were recorded. This is to see if there are any differences between materials with a low, medium, and high evaporation field, also spanning wider ranges of specimen voltages. Parts of these experiments were done on a LEAP 4000X HR in our lab in Erlangen. Since we assume that the electrostatics are identical between instruments of the same series, experiments were carried out at the Montanuniversität Leoben on a LEAP 3000X HR and a 5000 XR. Additional experiments were done on a LEAP 5000 XR and XS (straight flight path) at the University of Oxford and on the newest LEAP 6000 XR generation at Chalmers University of Technology. A summary of the experiments we performed and the resulting transformation files are provided in [Supplementary Table 1](#) and in the [Supplementary Material](#). The data analysis of the measurements with the grid electrode was performed first with IVAS or AP Suite, the analysis software of the instrument manufacturer, to extract the detector hit coordinates. Afterwards, the distortion mesh of the sample and the reflectron aberration correction are performed with the in-house-developed MATLAB toolbox in combination with 3D suite Blender (Blender). This MATLAB toolbox and the entire code are open sources and findable at GitHub ([Felfer, 2023](#)).

To assess the influence of the integration of a reflectron in one instrument series, in [Figure 2](#), two measurements on a LEAP 5000 XS (straight flight path, Fig. 2d) and 5000 XHR (reflectron, Fig. 2e) are compared. The detector hit coordinates (detx and dety) are analyzed with a histogram of the hit intensity on the detector, often referred to as field desorption map (FDM) shown in [Figures 2d](#) and [2e](#). Both samples are acquired with the grid electrode showing clearly low distortions for the straight flight path measurement and a distorted image of the grid for the reflectron-equipped instrument.

### Barycentric Transformation

The fundamental method used for the image correction in our case is that of an affine coordinate transform, facilitated by a barycentric coordinate transformation based on a piecewise linear approximation. This is a widely used method in computational image processing, whereby the coordinate of a point is related to an  $n$ -dimensional simplex, i.e., in a 2D triangle. The barycentric coordinates of a point with respect to that simplex are such that if the coordinates are interpreted as weights pulling down on the simplex vertices, the point would represent the center of mass, i.e., barycenter. If the coordinates of the simplex vertices are then transformed into a different space or shape, the barycentric coordinates equal a linear cotransformation. In our case, this is used on a mesh made from many triangles. These triangles are derived from image points in the field desorption pattern, caused by the grid that acts as a shadow mask in the physical detector space. The algorithm for this process is shown in [Figure 4](#). Since the actual shape of the shadow mask is known *a priori*, the transformation target from barycentric back to Cartesian into the virtual detector space is known. In [Figure 3](#), an example transformation is shown. In the Cartesian coordinate system is a red point  $h_1$  with the coordinates  $x_D$  and  $y_D$  in a blue triangle spanned by the points  $v_1$ ,  $v_2$ , and  $v_3$  of the measured grid. After the transformation into the barycentric system, the coordinates of point  $h_1$  are based on  $v_1$ ,  $v_2$ , and  $v_3$ . The actual shape of the shadow mask gives the triangle for the transformation from the barycentric back into the Cartesian system leading to the point  $h_1$  with the corrected detector hit coordinates  $x_{vD}$  and  $y_{vD}$ . Since an atom probe data set is a point cloud data set, the transformation is done for each ion.

### Extraction of the Image Distortions

To extract the image distortions, we employed a multistep process, based on the shadow image on the physical detector, shown in [Figure 4](#). In this process, we extract the crossing points of the grid image and use it as the basis for an affine transformation mesh. This mesh is extracted from the edges of the grid image rather than the crossing points to make it more robust against artifacts caused by variations in the image intensity. The basis is a 2D histogram of the detector hit intensity, also called FDM. It is fairly easy to extract the edges of the

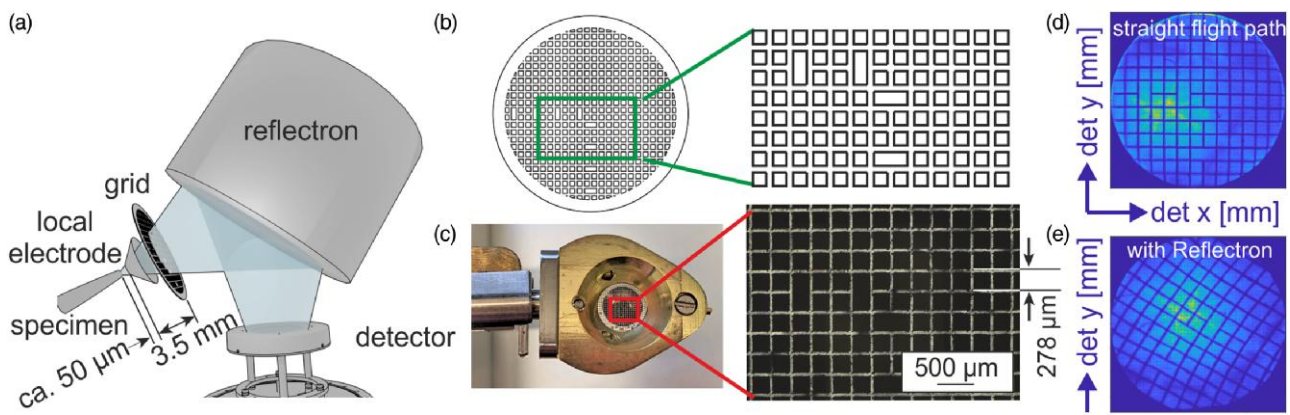


**Fig. 2.** Experiment setup for the determination of the imaging properties of the reflectron. (a) Position of the grid in the system. (b) Design of the grid and (c) installation in the counter electrode puck of the LEAP instrument showing an enlarged field of view that shows the alignment markers. (d) Field desorption map of a measurement from a straight flight path machine LEAP 5000 XS and (e) from an atom probe with a reflectron LEAP 5000 XHR, both instruments from the University of Oxford.

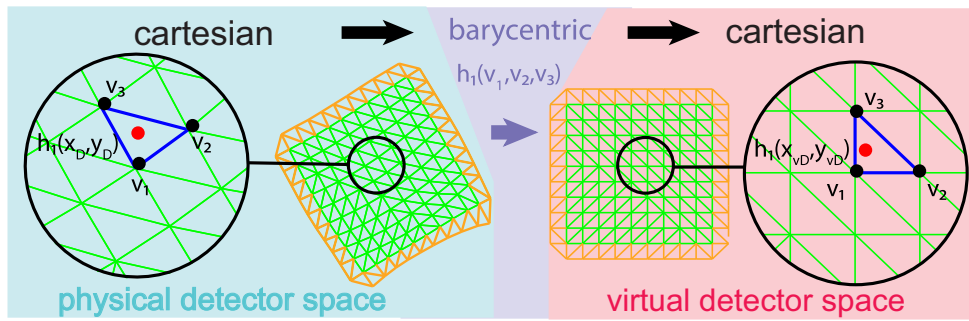


**Fig. 3.** Barycentric coordinate transformation of a point in its enclosing triangle in a mesh starting from a deformed mesh in the physical detector space into a rectilinear mesh in the virtual detector space.

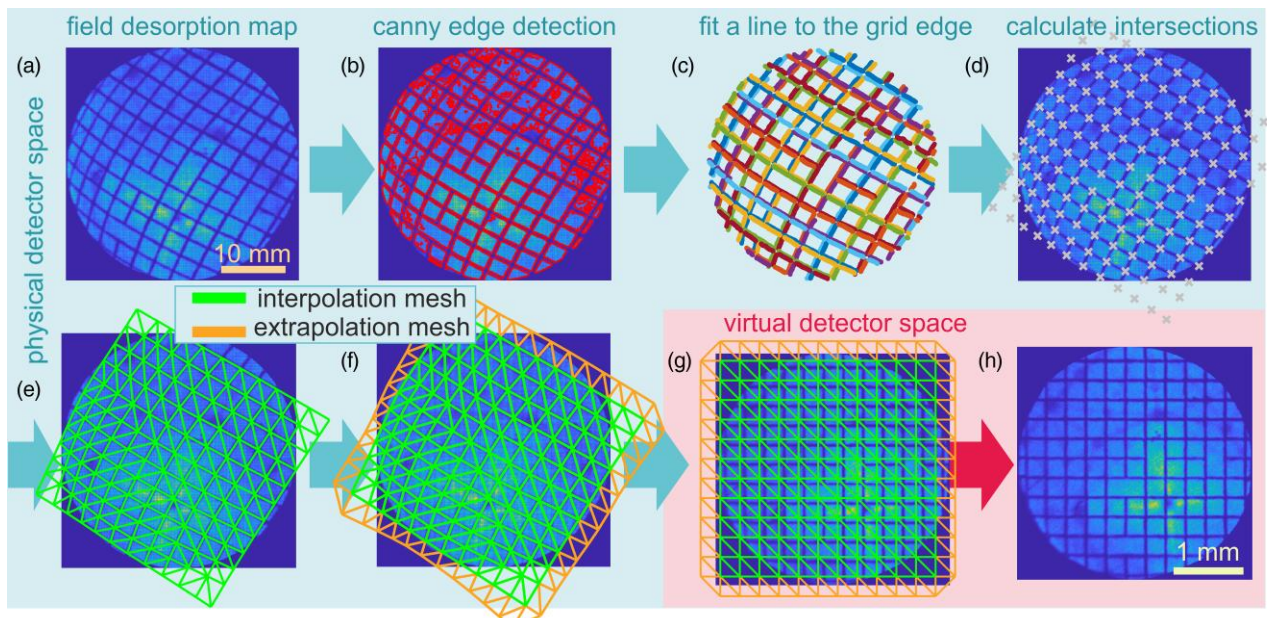


**Fig. 4.** Algorithm for extracting the reference mesh for the barycentric coordinates in physical detector space. (a) Detector histogram image showing an image of the calibration grid. (b) Canny edge detection of grid traces in the detector histogram image. (c) Manual identification of individual grid edges and fit calculation for each grid edge. (d) Extraction of the intersection points between individual grid bars. (e) Triangulation of these intersection points. (f) Extrapolation of grid edges. (g) Barycentric transformation of mesh and hit coordinates into virtual detector space. (h) FDM of hit coordinates in virtual detector space after the correction, the corrected FDM.

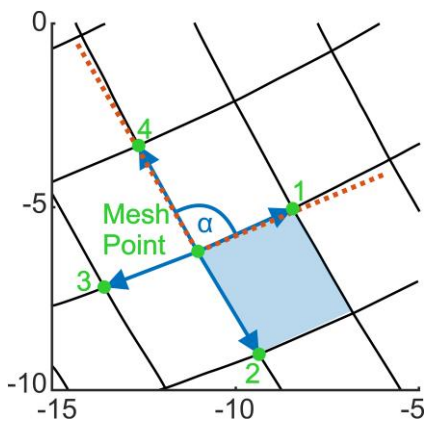


**Fig. 5.** Part of the mesh is shown with an exemplary MP to explain the calculation of area distortion, mesh skew angle, and mesh anisotropy. The fundamant of the calculation is the MP with its surrounding four points, marked as big dots, and their respective vectors. Two adjacent vectors span a quadrant, shown in the filled area. The sum of the four quadrants around the MP divided by the average value of the entire mesh is the area distortion for this MP. The mesh skew angle is the deviation of the angle  $\alpha$  between points 4 and 1 from  $90^\circ$ . The dotted lines are the vector addition of the two vectors with the same direction, P1-P3 and P4-P2. The ratio of them shows the mesh anisotropy of the mesh point.

grid in the FDM by binarizing the image at a threshold and using a Canny edge detection (Canny, 1986). This edge image will then contain the edges of the grid image and some artifacts caused by variations in hit density, e.g., caused by poles and zone lines. Therefore, we manually extract the grid edges and label them according to their distance to the grid origin. We used the 3D suite Blender 3.5 for this process (Blender Foundation, 2023).

The next step is then the extraction of the grid intersections. This is done by least-squares fitting a second-order spline to each of the grid lines and calculating their intersections. This makes the approach reasonably robust against local microscopic roughness of the calibration grid caused by the laser cutting process and aliasing of the image. The grid intersections are then determined to be at the mean location of the corner intersections of the grid edges. In the interior of the detector, this will be four corners, but at the edge of the detector, occasionally only one edge of a grid strip is on the detector. In this case, only two corners can be calculated, but their offset is taken into account. To enable an affine transformation based on barycentric coordinates, additionally a triangulation of the detector points is needed. Since not all edges are convex, we used an alpha hull and its interior triangulation (Edelsbrunner et al., 1983) with an alpha radius of 10 mm to avoid nonneighboring vertices being connected in the final triangulation.

While this can already be used as a basis for distortion calculations, the inclusion of detector hits outside the distorted square of grid lines captured on the detector requires an extrapolation of the location of the grid lines beyond the image. In the top right corner of Figure 4e, e.g., are detector hits lying outside the green interpolation mesh. During the correction, these hit coordinates will not be considered and corrected. To overcome this problem, we are placing the next set of grid intersection points at a distance given by a zeroth-order fit (i.e., same distance as neighboring grid row) of the grid intersection distances along the grid. In this extrapolation,

some distortions are present in the bottom corners of the grid. These do not matter however, since there are no detector data to be corrected in this part of detector space.

Based on the triangulated and extrapolated grid in Figure 4f, a transformation of the hit coordinates into “virtual detector space,” i.e., the plane of the shadow mask grid, is possible. This is done as a piecewise linear approximation of an affine transformation. The underlying assumption here is that a line of the length of one grid pitch or shorter can be approximated as only changing length, location, and rotation in the transformation but not curvature. For the grid pitch we used in the experiment, this seems reasonable. The transformation is then facilitated by transforming the physical Cartesian detector hit coordinates into barycentric coordinates relative to the mesh. Since the coordinates of the grid vertices are known, at least relative to the grid center, they can be used as a basis for the same triangulation, only with vertex coordinates at those known positions in the plane of the grid. The detector hit coordinates that were previously transformed into barycentric coordinates can then be retransformed into Cartesian coordinates in “virtual detector space” in the grid plane. The algorithms to calculate the transformation mesh as well as the calculated transformation meshes used in this paper are stored in the MATLAB toolbox (GitHub link).

During the calculation of the different FDMs for the LEAP instrument series (see Fig. 6), the LEAP 6000 XR showed a significantly different rotation of the grid’s shadow image. The data is rotated around  $60^\circ$  compared with the other instrument series. This rotation could be introduced by the ion optics, software, or a rotated detector. For the calculation of the intersection points of the LEAP 6000 data, the data set is therefore rotated by  $60^\circ$  to enhance zeroth-order fit. After the calculation, the data set and the intersection points are rotated back into the original coordinate system.

### Evaluation of the Image Distortions

To evaluate the image distortions of the individual instrument generations, for each mesh point (MP), the area distortion, mesh skew angle, and mesh anisotropy is calculated by using the four surrounding points, marked in green in Figure 5 and their vectors between the MP marked in blue. Two adjacent vectors span a rectangle. For each MP, this results in four surrounding areas which are not equal to the four surrounding rectangles of the mesh, shown in blue, the rectangle spanned by vectors 1 and 2. The sum of the four areas was calculated for each MP divided by the average value of the mesh to get the area distortion for this point. The mesh skew angle is the deviation of the angle  $\alpha$  between the vector of points 1 and 4 with the MP from  $90^\circ$ . For the mesh anisotropy, the ratio between the vector addition of vectors directing to opposite points around the MP (P1-P3 and P4-P2), marked in orange dotted line, is calculated.

### Application of the Method

For the end user, the application of the method is very simple, as it has no parameters that are specific to the experiment, only the instrument, as demonstrated below. To this end, we provide an implementation in MATLAB in the Supplementary Material, where the user loads the data in form of an \*.epos file; executes the barycentric transformation, with a transformation mesh specific to the instrument or instrument type; and is then free to use the corrected coordinates for

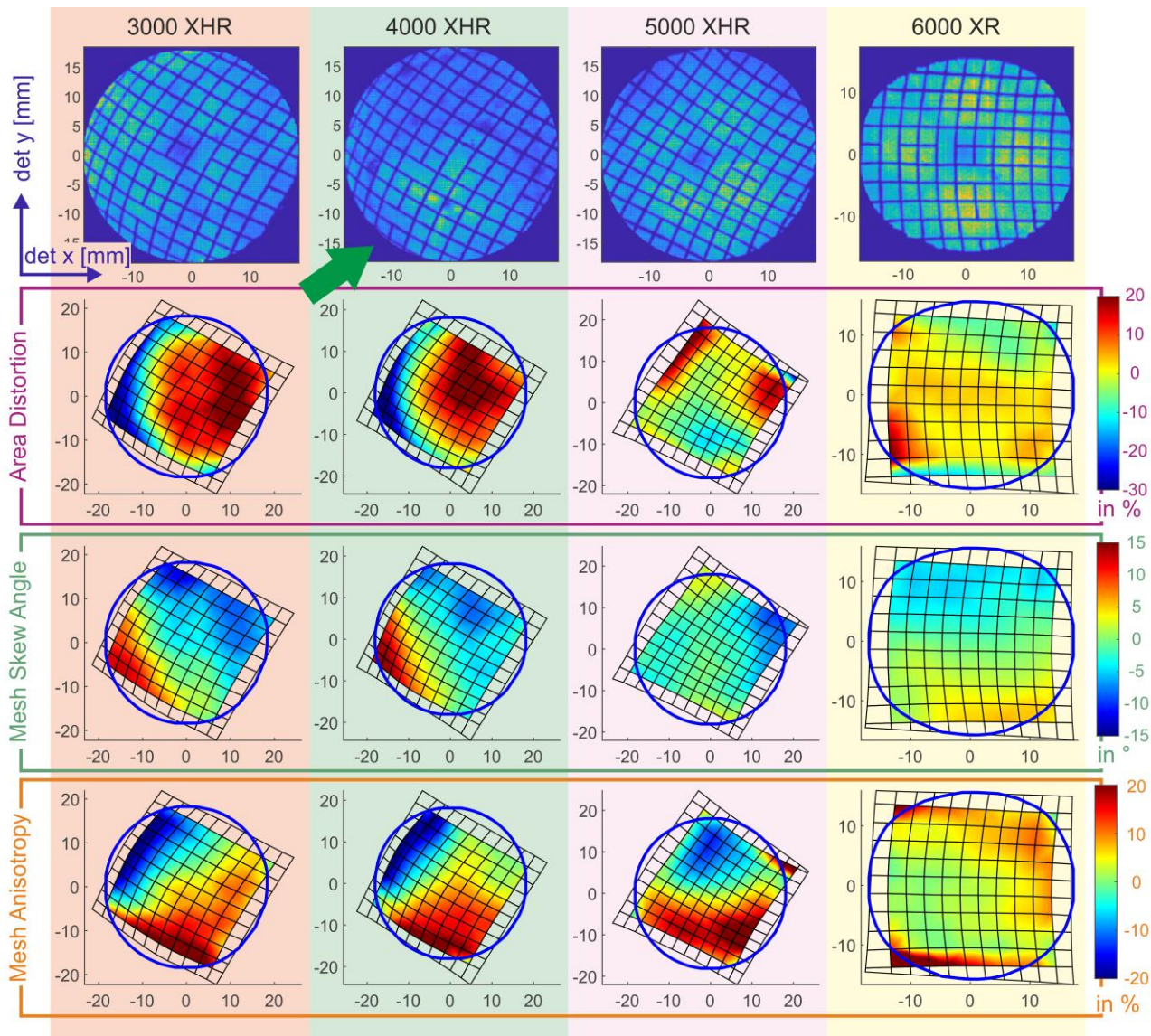


**Fig. 6.** Comparison between distortions on various LEAP series instruments. Measurements are done with Silicon on a LEAP 3000X HR (Montanuniversität Leoben), LEAP 5000 XR (Montanuniversität Leoben), and LEAP 6000 XR (Chalmers University of Technology). The data for the LEAP 4000X HR (FAU Erlangen-Nürnberg) are acquired with an Al tip. The incidence direction of the laser is shown by the green arrow. Shown are the FDMs with the projected grid together with the area distortion, the mesh skew angle, and the mesh anisotropy (see text for details).

further analysis. Reference data for all Imago/CAMECA instrument generations is also supplied. Mind that the transformation will only affect the detector hit coordinates and not the 3D reconstruction. However, new 3D reconstructions can be carried out on the transformed data. In the MATLAB toolbox (Felfer, 2023), we provide a MATLAB implementation of the reconstruction protocol for wide-angle atom probes after Geiser (Gault et al., 2011a).

## Results and Discussion

### Comparison of Different Atom Probe Systems

Even without applying image transformation, we can compare imaging properties between different instrument types and individual instruments of the same type using the transformation mesh. Figure 6 shows a comparison of imaging properties of various instruments from different Imago/CAMECA LEAP generations. From the curvature of the grid in the

FDMs, the different distortion meshes for different LEAP generations are calculated. For a quantitative comparison, histograms of the area distortion, mesh skew angle, and mesh anisotropy were calculated including the maximum, minimum, and standard deviation (Fig. 7) using the intersection points that lie in the FDM.

When comparing the LEAP instrument generations, it is noticeable that the 3000 and 4000 are very similar and there is a generational development step to the LEAP 5000 device and again another step to the LEAP 6000 device. Highly similar distortion maps in Figure 6 as well as comparable histograms with maximum, minimum, and standard deviation (Fig. 7) are an indication for the similarity of the LEAP 3000 and LEAP 4000 reflectrons. Both instruments introduce similar distortions in the data set. A closer look to the standard deviation of the LEAP 5000 and 6000 distortion grid shows a reduced standard deviation, compared to the other devices. That is the case for the LEAP 6000 instrument for the area distortion,

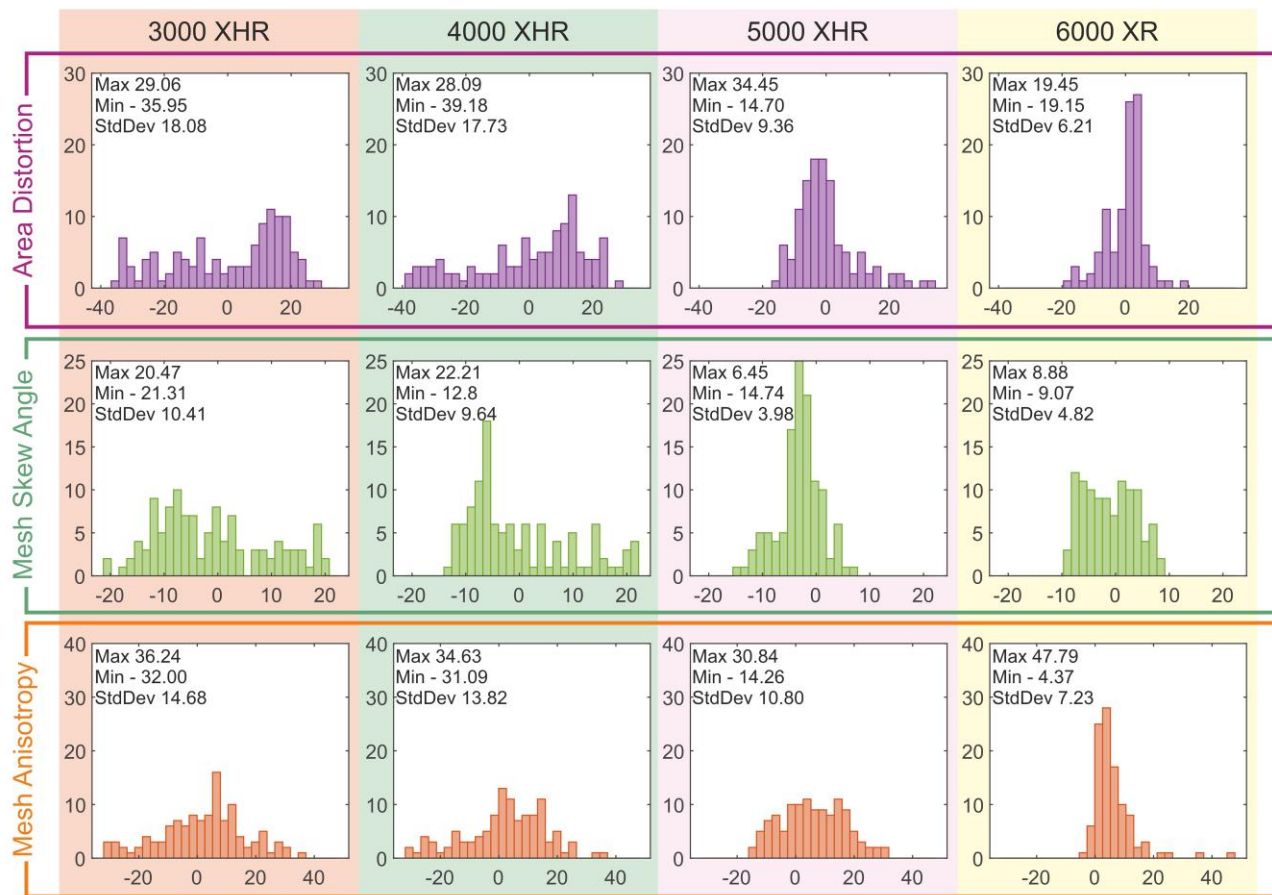


**Fig. 7.** This figure shows the histogram of the area distortion, the mesh skew angle, and the mesh anisotropy calculated for each atom probe instrument generation.

mesh skew angle, and mesh anisotropy. For the area distortion and mesh anisotropy, the histogram shows additional the highest frequency. Consequently, the mesh of the LEAP 6000 device introduces the lowest area distortion and has the lowest anisotropy. Interestingly, the LEAP 5000 instrument has the lowest standard deviation for the mesh skew angle, and the histogram shows the highest frequency. Therefore, the mesh of the 5000 generation is the one with the lowest deviation of the angles from 90°.

### Influence of Evaporation Field

In order to assess the influence of the evaporation field of the specimen, we carried out experiments on Al (low field/low experiment voltages, Fig. 8a) and W (high field/high experiment voltages, Fig. 8b). The results of these experiments are shown in Figures 8a and 8b. Here, the images of the mesh grid for each experiment show no difference in area distortion, mesh skew angle, and mesh anisotropy. This was to be expected if the electrostatic potential of the reflectron is well matched to the field evaporation potential of the specimen. Different materials were measured on LEAP 4000, 5000, and 6000 instruments and are superimposed and displayed in Figures 8c to 8e. The grids show nearly the same deformation in shape. It leads us to the conclusion that the image distortions in the data as presented to the user are universal for all materials measured in reflectron LEAP systems, and thus, one single conversion can be used for all specimens on one instrument. There is

only a slight offset in the grid positions due to different specimen alignments. The intrasystem consistency of the distortions is demonstrated in Figure 8d. Here, we are comparing the data from two different instruments of the same LEAP 5000 generation. W tips are measured at the instrument in the University of Oxford atom probe group, and Si was measured at the Montanuniversität Leoben. The superimposed grids show the same shape. This demonstrated the consistency of the distortions between two different instruments of the same reflectron generation. This suggests that only one “master” calibration file for one instrument generation would be required. This will need to be proven for the other instrument generations by more measurements and is beyond the scope of this paper. With this method, each research group equipped with an atom probe can make their own calibration grid for their instrument.

### Application of Transformation to the Point Cloud

Using the known shape of the shadow mask grid and its image on the detector, we can now use the affine transformation to “un-distort” the detector coordinates of data sets that have been recorded without the grid inserted. This is by using the barycentric transformation introduced above. MATLAB code for this operation is included in the [Supplementary Material](#) (Workflow\_ReflectronCorrection\_Dataset mlx) and in the MATLAB analysis toolbox ([Felfer, 2023](#)), as well as reference transformation data for LEAP 3000X HR, 4000X HR,

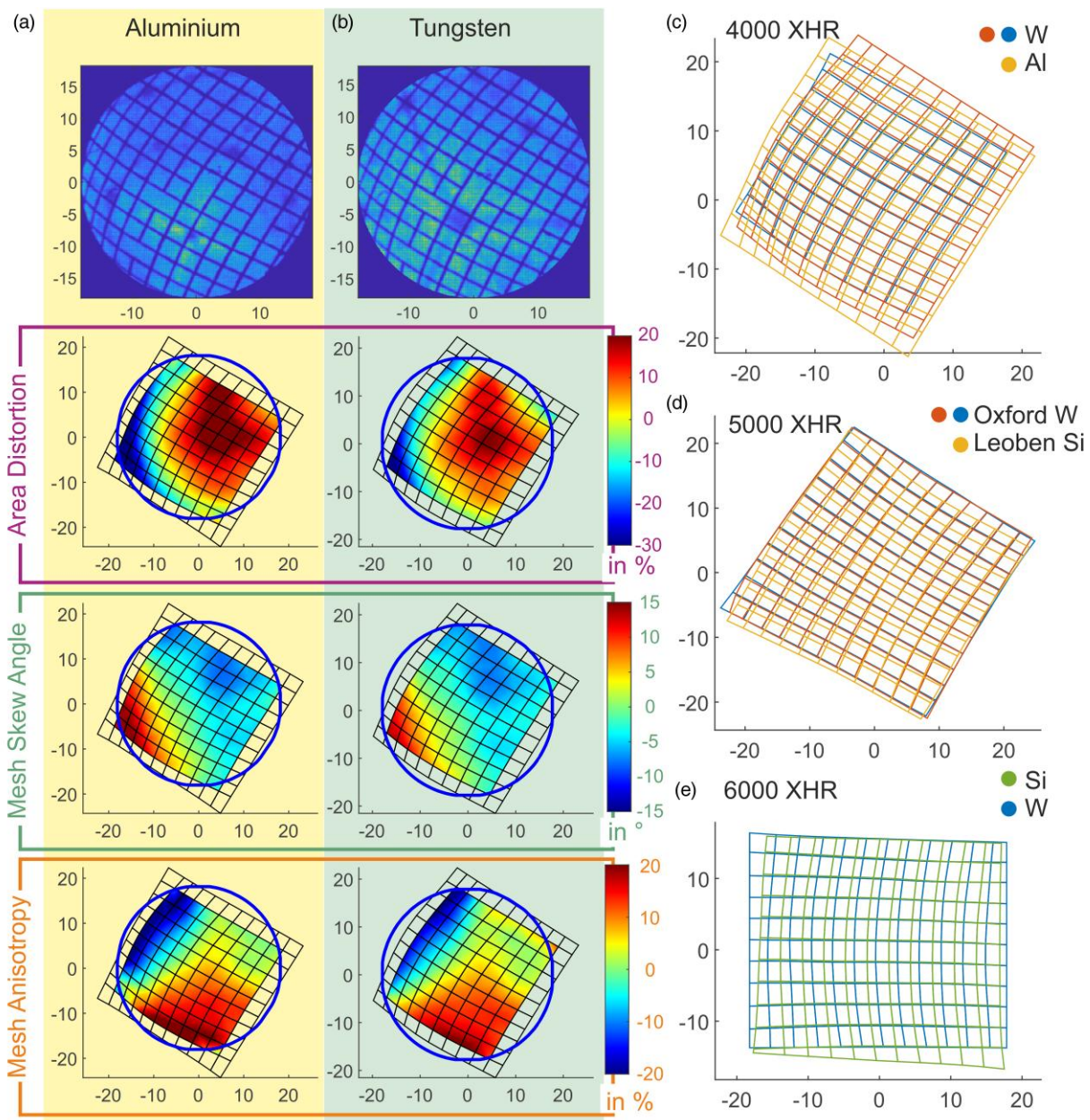


**Fig. 8.** Influence of different materials and different instruments of the same generation on the distortion mesh. **(a,b)** show two different measurements acquired with the grid electrode at the LEAP 4000X HR in Erlangen-Nürnberg; sample **(a)** is Al and **(b)** is W. **(c,e)** show mesh grid overlay images of different materials and **(d)** also acquired with two different LEAP 5000 instruments (Montanuniversität Leoben, University of Oxford).

5000 XR, and 6000 XR series reflectron instruments. This allows the reader to perform the transformation with only the data itself and suitable reference transformation data as the input.

As an example, we have carried out a reflectron correction for Al, recorded on the LEAP 4000X HR in the Erlangen APT lab. We have ended the experiment with the specimen still intact and transferred the specimen into the titanium atom probe in the same lab (Felfer et al., 2022) for comparison. This instrument has a straight flight path configuration and thus only a uniform image compression at least caused by the instrument (Gault et al., 2011b; Felfer & Cairney, 2016). Pure Al was chosen as it exhibits many poles and zone lines, which enable an easy visual assessment of the image distortions. In Figure 9a, the FDM, calculated from the detx

and dety coordinates provided by IVAS, is displayed. The white line between the poles (101) and (111) shows the actual zone line with a curvature. After applying the reflectron correction to the data set, the zone line shown in Figure 9b is straight with no distortion like the FDM acquired with a straight flight path instrument in Figure 9c.

The shift in orientation stems from using the grid orientation as the reference. This can be put in reference to any other directions such as the specimen orientation in the puck or the laser incident direction. By applying the affine transformation as a reflectron correction, the resulting data can thus be treated as if it was collected on an instrument with straight flight path going forward. Of course, the detector hit coordinates are then relative to a “virtual detector” in the plane where the calibration grid was positioned and relative to the

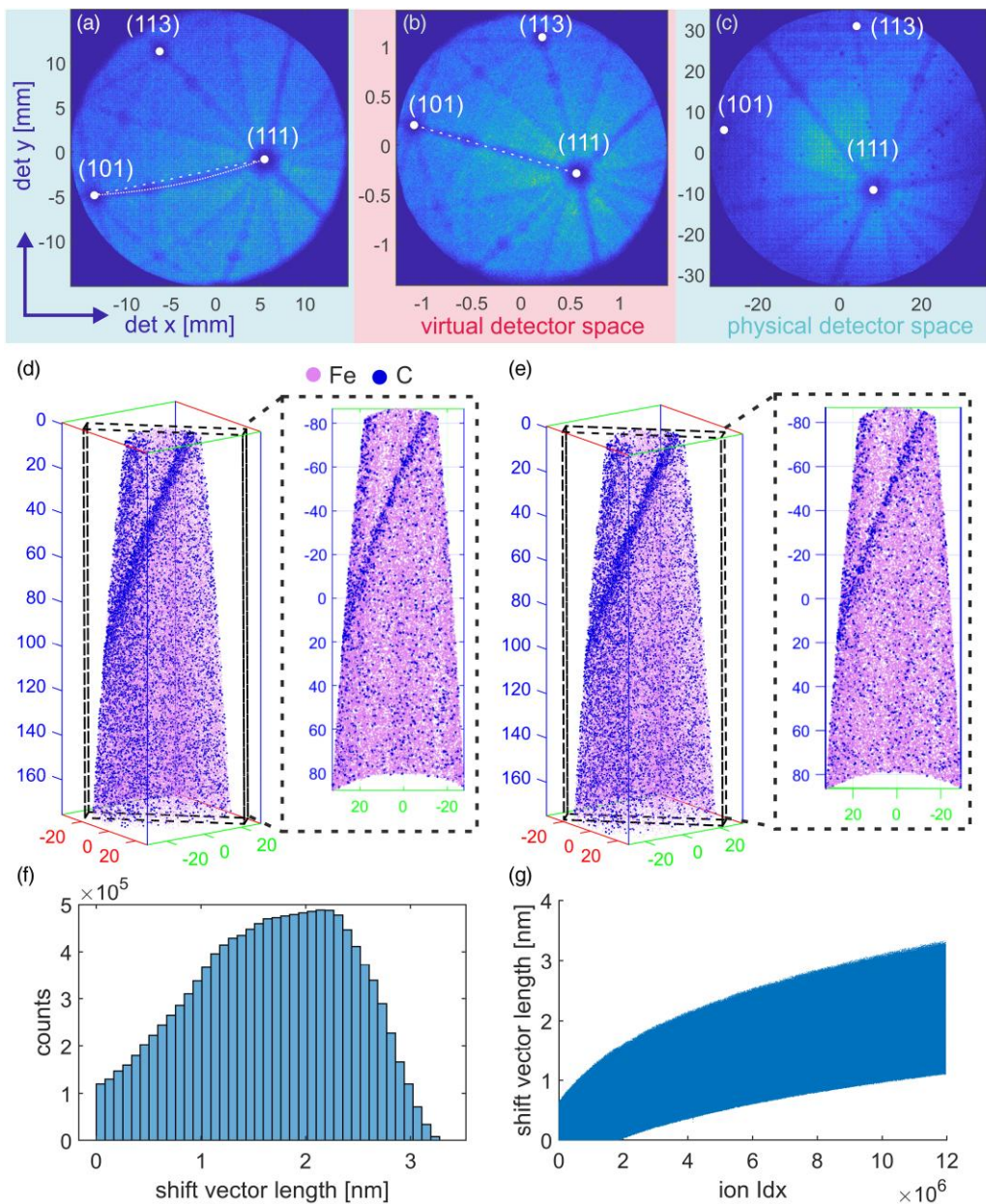


**Fig. 9.** **(a,b)** Field desorption map of the same measured Al tip **(a)** with no correction measured at the LEAP 4000X HR, **(b)** with the reflectron correction, and **(c)** the same tip measured with a custom-designed straight flight path instrument (Felfer et al., 2022). **(d,e)** Both reconstructions show the same measurement of an iron tip with a grain boundary. The carbon segregates at the grain boundary. **(d)** Reconstruction after IVAS, plotted by the MATLAB toolbox. **(e)** Reconstruction after reflectron distortion correction, subsequently reconstructed after Geiser (Gault et al., 2011a) and plotted in MATLAB. Reconstruction parameters: **(e)** in IVAS, flight path 382 mm;  $k_f = 3.3$ ; ICF = 1.4; FeVap 33.49 V/nm; for MATLAB reconstruction workflow, flight path 3.5 mm;  $k_f = 3.93$ ; ICF = 1.31; FeVap 33 V/nm. **(f,g)** show the shift vector length as a histogram **(f)** and over ion index **(g)**.

coordinate of this grid. If this data is then used to create 3D APT reconstructions, the reconstruction parameters used, e.g., in Bas-type reconstructions (Bas et al., 1995; Larson et al., 2013), like the image compression factor (ICF) or flight distance, may lose some of their physical meaning but can still be determined in established ways (Gault et al., 2009). In Figures 9d and 9e, we show a comparison of a reconstruction done using the proprietary CAMECA IVAS 3.6 software (Fig. 9d) and one with our own implementation of the reconstruction protocol after Geiser (Gault et al., 2011a). This reconstruction protocol is, e.g., implemented in the MATLAB analysis toolbox provided by the Erlangen APT group (Felfer, 2023).

In Figures 9d and 9e, another atom probe data set is reconstructed with IVAS and also with MATLAB after the reflectron correction. The analyzed sample is high-purity iron (99.99%, HMW Hauner GmbH & Co.KG) with a large grain size ( $>100 \mu\text{m}$ ). A scanning electron microscope and a focused ion beam with the lift-out method introduced in Felfer et al. (2012) were used to prepare the APT specimen. A grain boundary with carbon dispersed is visible inside the tip. For the reconstruction, the evaporation field of 33 V/nm used by IVAS is used for both reconstructions. In IVAS, the flight path length of 382 mm, a field factor ( $k_f$ ) of 3.3, and the ICF of 1.4 were chosen to get a flat grain boundary in the reconstruction. For the reconstruction implementation in

**Table 1.** Reconstruction Parameters Used in IVAS and MATLAB, Calculated Volume of Reconstructed Tips, and the Volume Difference in Percentage.

	Flight Path Length (mm)	ICF	$k_f$	Volume ( $\text{nm}^3$ )
IVAS	382	1.4	3.3	$3.19 \times 10^5$
MATLAB	3.5	1.31	3.93	$3.22 \times 10^5$
Difference				0.89%

MATLAB analysis toolbox, we used the reconstruction protocol after Geiser (Gault et al., 2011b). In order to obtain, a reconstructed data set as similar as the one reconstructed by IVAS, we used the volume and the maximum z-height of the reconstructed tip to fit our reconstruction to the one provided by IVAS by optimizing the values for the ICF and the  $k_f$  and rigid body shift and rotation. The flight path in the virtual detector space is the physical distance between the tip and the grid of 3.5 mm in the reference counter electrode setup. In a regular measurement, the grid is not present. Consequently, we use the height of the electrode cone as flight path length, because the grid is placed directly under the electrode cone (see Fig. 2). The distance between the tip and the electrode is in the order of 50  $\mu\text{m}$  and thus negligible. The next parameter that had to be adjusted for the reconstruction was the effective detector area. Each individual specimen has its own effective detector area since the detector is often not entirely filled. By varying this parameter, the difference in volume between the two data sets is minimized. Volume calculation was done in MATLAB for both data sets with the same range file and same atomic volumes. The best value for the effective detector area for the here presented data set was 5.51  $\text{mm}^2$  followed by an adjacent optimization of the ICF of 1.31 and a  $k_f$  of 3.93. The goal of the parameter optimization was to keep the volume difference at a minimum and a maximum difference in z-height with  $\pm 2$  nm. All results are presented in Table 1, and the volume difference was minimized to 0.89%.

To compare the two reconstructions in detail, we calculated the spatial shifts between the positions of individual ions in both reconstructions. After the reflectron correction, the data set is rotated, because the initial grid for the back transformation is straight as seen in Figure 2. By varying the rotation angle stepwise and calculating the maximum shift vector between the ions of both data sets for each angle, the optimum rotation angle with the minimum shift vector is found to be 30.3°. Figure 9f shows the frequency distribution of the different lengths of the shift vector, and the evolution over the ion index number is shown in Figure 9g. After the reflectron correction and the adjacent reconstruction, the data set shows a maximum shift vector of 3.34 nm with a mean value of 1.6 nm. More than 90% of the ions are less than 2.6 nm away. This amounts to only around 4% of the lateral data set size. With increasing ion index number in z direction, the shift vector length is also increasing due to the higher radius of the tip. In any independent reconstruction, the parameters would be determined on physically known properties of the specimen investigated and the parameters would adjust accordingly.

## Conclusions

Modern wide-angle reflectron atom probes have a high mass resolution, but they come with the disadvantage that the reflectron always introduces distortions into the data set. Due

to the proprietary nature of the instrument design, the imaging properties of the reflectron mirrors were unknown to the user. This prohibits researchers from creating their own reconstruction protocols in a meaningful way or performing analysis such as APT crystallography. With the presented experimental approach, it is possible to generate an affine transformation, based on a mesh with known geometry, to transform the provided detector data to a virtual detector situated before the reflectron. 3D reconstructions and other analyses analogous to straight flight path instruments can then be performed with the newly calculated detector hit coordinates.

To calculate the affine transformation for a certain instrument, one atom probe measurement with an installed reference grid inside the used local electrode is needed. Our measurements on a number of different materials and different instruments have indicated that the affine transformation mostly depends on the instrument type. Any dependencies on material and specific instrument seem minor. This allows us to supply reference files for all currently common reflectron instruments (LEAP 3000, 4000, 5000, and 6000 series). These reference files are provided in the Supplementary Material together with all code used in this paper.

## Availability of Data and Materials

The authors have declared that no data sets apply for this piece.

## Supplementary Material

To view supplementary material for this article, please visit <https://doi.org/10.1093/mam/ozae052>.

## Acknowledgments

The authors would like to thank Martin Meier at the University of Oxford for measurements on the LEAP 5000 XR system. Ronald Schnitzer and Michael Tkadletz of the Montanuniversität Leoben are appreciated for measurements with the grid electrode on the LEAP 3000X HR and 5000 XR system. The data of the LEAP 6000 XR were thankfully acquired by Mattias Thuvander and Jakob Severin of the Chalmers University of Technology.

## Financial Support

This work has received funding from the European Research Council (ERC) under the European Union's Horizon 2020 Research and Innovation Programme (Grant Agreement No. 805065).

## Conflict of Interest

The authors declare that they have no competing interest.

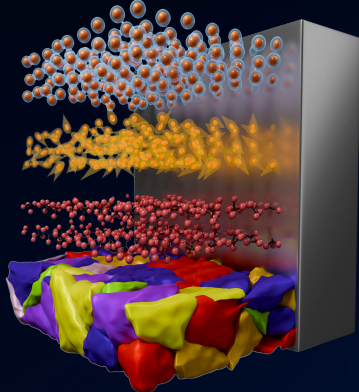
## References

- Bas P, Bostel A, Deconihout B & Blavette D (1995). A general protocol for the reconstruction of 3D atom probe data. *Appl Surf Sci* 87–88, 298–304. [https://doi.org/10.1016/0169-4332\(94\)00561-3](https://doi.org/10.1016/0169-4332(94)00561-3)
- Beinke D, Oberdorfer C & Schmitz G (2016). Towards an accurate volume reconstruction in atom probe tomography. *Ultramicroscopy* 165, 34–41. <https://doi.org/10.1016/j.ultramic.2016.03.008>
- Blavette D, Bostel A, Sarrau JM, Deconihout B & Menand A (1993). An atom-probe for 3-dimensional tomography. *Nature* 363, 432–435.

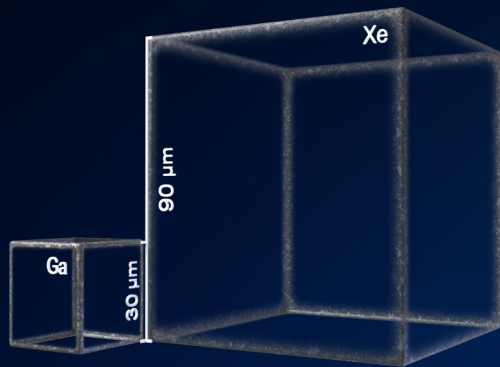
- Blender Foundation (2023). Blender. Available at <https://www.blender.org/> (retrieved March 29, 2023).
- Canny J (1986). A computational approach to edge detection. *IEEE Trans Pattern Anal Mach Intell PAMI* 8, 679–698. <https://doi.org/10.1109/TPAMI.1986.4767851>
- Cerezo A, Godfrey TJ, Sijbrandij SJ, Smith GDW & Warren PJ (1998). Performance of an energy-compensated three-dimensional atom probe. *Rev Sci Instru* 69, 49–58. <https://doi.org/10.1063/1.1148477>
- Edelsbrunner H, Kirkpatrick D & Seidel R (1983). On the shape of a set of points in the plane. *IEEE Trans Inform Theory* 29, 551–559. <https://doi.org/10.1109/TIT.1983.1056714>
- Felfer PJ (2023). Atom probe toolbox. Available at <https://github.com/peterfelfer/Atom-Probe-Toolbox> (retrieved March 2, 2023)..
- Felfer PJ, Alam T, Ringer SP & Cairney JM (2012). A reproducible method for damage-free site-specific preparation of atom probe tips from interfaces. *Microsc Res Tech* 75, 484–491. <https://doi.org/10.1002/jemt.21081>
- Felfer P & Cairney J (2016). A computational geometry framework for the optimisation of atom probe reconstructions. *Ultramicroscopy* 169, 62–68. <https://doi.org/10.1016/j.ultramic.2016.07.008>
- Felfer P, Ott B, Monajem M, Dalbauer V, Heller M, Josten J & Macaulay C (2022). An atom probe with ultra-low hydrogen background. *Microsc Microanal* 28, 1255–1263. <https://doi.org/10.1017/S1431927621013702>
- Fletcher C, Moody MP, Fleischmann C, Dialameh M, Porret C, Geiser B & Haley D (2022). Automated calibration of model-driven reconstructions in atom probe tomography. *J Phys D: Appl Phys* 55, 375301. <https://doi.org/10.1088/1361-6463/ac7986>
- Gault B, Haley D, de Geuser F, Moody MP, Marquis EA, Larson DJ & Geiser BP (2011a). Advances in the reconstruction of atom probe tomography data. *Ultramicroscopy* 111, 448–457. <https://doi.org/10.1016/j.ultramic.2010.11.016>
- Gault B, Loi ST, Araullo-Peters VJ, Stephenson LT, Moody MP, Shrestha SL, Marceau RKW, Yao L, Cairney JM & Ringer SP (2011b). Dynamic reconstruction for atom probe tomography. *Ultramicroscopy* 111, 1619–1624. <https://doi.org/10.1016/j.ultramic.2011.08.005>
- Gault B, Moody MP, Cairney J & Ringer S (2012a). *Atom Probe Microscopy*. New York: Springer.
- Gault B, Moody MP, Cairney JM & Ringer SP (2012b). Atom probe crystallography. *Materials Today* 15, 378–386. [https://doi.org/10.1016/S1369-7021\(12\)70164-5](https://doi.org/10.1016/S1369-7021(12)70164-5)
- Gault B, Moody MP, de Geuser F, Tsafnat G, La Fontaine A, Stephenson LT, Haley D & Ringer SP (2009). Advances in the calibration of atom probe tomographic reconstruction. *J Appl Phys* 105, 034913. <https://doi.org/10.1063/1.3068197>
- Gault B, Vurpillot F, Vella A, Gilbert M, Menand A, Blavette D & Deconihout B (2006). Design of a femtosecond laser assisted tomographic atom probe. *Rev Sci Instru* 77, 43705. <https://doi.org/10.1063/1.2194089>
- Kellogg GL & Tsong TT (1980). Pulsed-laser atom-probe field-ion microscopy. *J Appl Phys* 51, 1184–1193. <https://doi.org/10.1063/1.327686>
- Kelly TF, Camus PP, Larson DJ, Holzman LM & Bajikar SS (1996). On the many advantages of local-electrode atom probes. *Ultramicroscopy* 62, 29–42. [https://doi.org/10.1016/0304-3991\(95\)00086-0](https://doi.org/10.1016/0304-3991(95)00086-0)
- Larson DJ, Gault B, Geiser BP, De Geuser F & Vurpillot F (2013). Atom probe tomography spatial reconstruction: Status and directions. *Curr Opin Solid State Mater Sci* 17, 236–247. <https://doi.org/10.1016/j.cossms.2013.09.002>
- Ling Y-T, Cools S, Bogdanowicz J, Fleischmann C, Beenhouwer JD, Sijbers J & Vandervorst W (2022). A bottom-up volume reconstruction method for atom probe tomography. *Microsc Microanal* 28, 1102–1115. <https://doi.org/10.1017/S1431927621012836>
- Meisenkothen F, Kelly TF, Oltman E, Bunton JH, Renaud L & Larson DJ (2016). Using mass resolving power as a performance metric in the atom probe. *Microsc Microanal* 22, 680–681. <https://doi.org/10.1017/S1431927616004256>
- Müller EW, Panitz JA & McLane SB (1968). The atom-probe field ion microscope. *Rev Sci Instru* 39, 83–86. <https://doi.org/10.1063/1.1683116>
- Nishikawa O & Kimoto M (1994). Toward a scanning atom probe—computer simulation of electric field. *Appl Surf Sci* 76–77, 424–430. [https://doi.org/10.1016/0169-4332\(94\)90376-X](https://doi.org/10.1016/0169-4332(94)90376-X)
- Panayi P (2006). Atom Probe, WO 2006/134380 A2, PCT/GB2006/002209.
- Poschenrieder WP (1972). Multiple-focusing time-of-flight mass spectrometers part II. TOFMS with equal energy acceleration. *Int J Mass Spectromet Ion Phys* 9, 357–373. [https://doi.org/10.1016/0020-7381\(72\)80020-2](https://doi.org/10.1016/0020-7381(72)80020-2)
- Waugh AR, Richardson CH & Jenkins R (1992). APFIM 200—A reflectron-based atom probe. *Surf Sci* 266, 501–505. [https://doi.org/10.1016/0039-6028\(92\)91066-K](https://doi.org/10.1016/0039-6028(92)91066-K)

# TESCAN AMBER X2

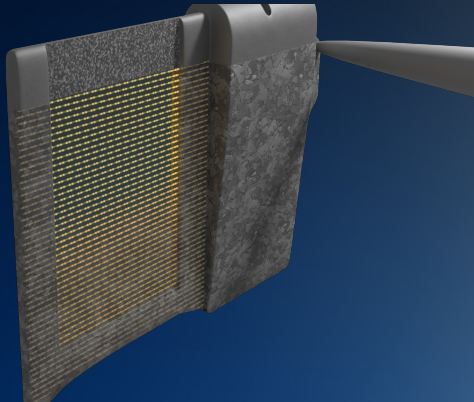
## PLASMA FIB-SEM REDEFINED



**UTILITY  
REDEFINED**



**SPEED  
REDEFINED**



**PRECISION  
REDEFINED**

[info.tescan.com](http://info.tescan.com)